Int. J. Electrochem. Sci., 12 **(2017)** 12084 – 12097, doi: 10.20964/2017.12.400

International Journal of
ELECTROCHEMICAL
SCIENCE
www.electrochemsci.org

Nitrogen Self-Doped Porous Carbon Materials Derived from a New Biomass Source for Highly Stable Supercapacitors

Zhenjie Sun[1,2,*], *Jianghan Liao*[1], *Bo Sun*[1], *Meiling He*[1], *Xiang Pan*[1],*Jiping Zhu*[1,2], *Chengwu Shi*[1,3,*], *Yang Jiang*[2]

[1] Department of Chemical Engineering and Food Processing/Mechanical Engineering, HeFei University of Technology, Xuancheng 242000, P.R. China
[2] School of Materials Science and Engineering, HeFei University of Technology, Hefei 230009, P.R. China
[3] School of Chemistry and Chemical Engineering, HeFei University of Technology, Hefei 230009, P.R. China
[*]E-mail: sunzhenjie2008@126.com, shicw506@foxmail.com

Received: 30 August 2017 / *Accepted:* 31 October 2017 / *Online Published:* 12 November 2017

Nitrogen self-doped porous carbon materials with large surface area and excellent cycle stability are successfully synthesized from the waste of *Pteroceltis tatarinowii* Maxim (PTM) bark for the first time. During the synthesis procedure, ethanol is introduced to ensure a homogeneous mixture and good contact of the precarbonized PTM bark with the activating agent (KOH or $ZnCl_2$), resulting in a unique porous structure. The obtained KOH activated carbon (K-AC) possesses a hierarchical porous structure with a high specific surface area of 1721 m^2 g^{-1} and small amount of nitrogen (0.3 wt%). Interestingly, $ZnCl_2$-activated carbon (Zn-AC) shows a micropore structure with a narrow pore size distribution (0.5–2.0 nm) and a higher nitrogen content of 3.0 wt%. The electrochemical measurement results demonstrate that the as-prepared Zn-AC exhibits a high specific capacitance of 206 F g^{-1} at a current density of 0.5 A g^{-1}, good rate performance and excellent cycle stability with capacitance retention of 99% over 10,000 cycles. In contrast, K-AC retains only approximately 89% of the initial capacitance value after 10,000 cycles. Thus, such waste PTM bark-derived carbon material, obtained by the $ZnCl_2$ activated method, is a promising candidate material as an electrode for highly stable supercapacitors.

Keywords: Porous carbon; Nitrogen self-doping; Electrode material; Supercapacitor; Cycle stability

1. INTRODUCTION

Supercapacitor, also called ultracapacitor, is considered one of the most promising energy storage devices owing to its higher energy density compared with conventional electric double-layer capacitors, and faster charge-discharge rate and more excellent cycle stability than secondary lithium-ion batteries [1,2]. To further enhance the electrochemical performance of supercapacitors, researchers in this field have mainly focused on electrode materials, which is one of the most important factors that determine the performance of supercapacitors. It is well known that the electrode materials for supercapacitor application mainly include carbon materials, transition metal oxides and conducting polymers. Among them, porous carbon is an attractive electrode material for supercapacitor application because of its high specific surface area, good chemical stability, high electrical conductivity, and abundant resources [3-5]. Generally, porous carbon materials are believed to function as electrical double layer capacitors (EDLCs), which store energy through the electrostatic adsorption of electrolyte ions at the electrode and electrolyte interface [1,6]. Based on the energy storage mechanism, the charge accumulation on the carbon electrode depends strongly on the surface area, pore size distribution and total pore volume [7,8]. Therefore, a large number of porous carbon materials with large specific surface area, high pore volume and optimized pore size distribution have been synthesized and studied for supercapacitor application [9-19]. However, it is a challenge to further improve the specific surface areas of carbon materials using current method and technology. Moreover, even if the carbon materials possess a high specific surface area, the surface area does not fully contribute to the capacitance, as a certain number of random pores in carbon materials are generally inaccessible to electrolyte ions [20].

Heteroatom doping can increase the surface wettability, electronic conductivity and electroactive surface area of carbon materials, and heteroatoms (such as N, O, S and B) have been introduced into carbon materials to enhance the electrochemical performance [21-31]. However, the traditional heteroatom functionalization needs to add a certain amount of heteroatom sources and normally coupled with increasing cost and instable cycle performance. Therefore, it is of great significance to explore a facile and low-cost method to prepare heteroatom-doped carbon materials with high capacitance and long cycling stability. Biomass materials generally possess unique elaborate structures and various functional groups, which are beneficial for the synthesis of heteroatom self-doped carbon materials with a unique structure [32]. Thus, biomass-derived carbon electrode materials for high-performance supercapacitors have garnered more and more research interest in recent years [33-37]. For example, Cao *et al*. [33] synthesized nitrogen-doped hierarchical porous carbon nanosheets from natural silk. The obtained carbon showed a specific capacitance of 242 F g^{-1} at 0.1 A g^{-1} and high cycling stability (91% retained after 10,000 cycles). Xie *et al*. [34] reported a grass-derived heteroatom-doped hierarchical porous carbon, which exhibited a high specific capacitance of 336 at 1 A g^{-1}, and the capacitance remained approximately 88% after 2000 cycles. In the work of Liu *et al*. [35], *Platanus* seed fibres were selected to synthesize sulfur-nitrogen dual doped hierarchical porous carbon materials, which possessed a high specific capacitance of 287 F g^{-1} at 0.25 A g^{-1} and an excellent capacity retention of 97% after 10,000 cycles. Notably, the biomass-derived carbon materials exhibit superior electrochemical properties.

Herein, we propose a new biomass source for preparing nitrogen self-doped carbon materials. *Pteroceltis tatarinowii* Maxim (PTM) is one of the Chinese endemic fibre plants, and its bark is the best source for the manufacture of Xuan paper. In this work, carbon materials were prepared using the waste of PTM bark from the Xuan paper manufacturing process as a precursor and KOH or $ZnCl_2$ as an activating agent. To ensure a homogeneous mixture and good contact of the precarbonized PTM bark with the activating agent, ethanol was introduced to mix the precarbonized PTM bark with KOH or $ZnCl_2$, resulting in a high specific surface area and unique porous structure. The obtained KOH activated carbon (K-AC) possesses a hierarchical porous structure with high specific surface area, high pore volume and small amount of nitrogen. Interestingly, compared with K-AC, $ZnCl_2$ activated carbon (Zn-AC) shows a micropore structure with a narrow pore size distribution and higher nitrogen content. The electrochemical measurement results demonstrate that the as-prepared Zn-AC possesses a higher rate capability and more excellent cycling stability than K-AC. Thus, such waste PTM bark-derived carbon material, obtained by the $ZnCl_2$ activated method, is a promising electrode material for high-performance supercapacitors.

2. EXPERIMENTAL

2.1. Preparation of Zn-AC and K-AC

The waste of PTM barks was collected from a Xuan paper making factory and then washed with deionized water and dried at 80 °C for 24 h in an oven. The dried PTM barks were precarbonized at 300 °C for 3 h at a heating rate of 1 °C min^{-1}. The obtained precarbonized PTM barks were ground and then mixed with $ZnCl_2$ or KOH at a weight ratio of 1:1 in ethanol. The obtained mixtures were stirred for 12 h at room temperature, then dried at 100 °C in an oven and carbonized in a tubular furnace at 900 °C for 2 h with a heating rate of 3 °C min^{-1} under a nitrogen atmosphere. The obtained products were treated with 1 M HNO_3 aqueous solution three times, washed several times using deionized water and vacuum dried at 80 °C for 24 h. The final products were labeled as Zn-AC and K-AC, respectively.

2.2. Materials characterization

The crystallographic information of the carbon materials was characterized by powder X-ray diffraction (XRD) using a Smartlab9 X-ray generator in which Cu Ka was used as the radiation source. The specific surface area and pore size distribution of the samples were observed by a surface area analyzer (Autosorb-iQ2-MP). The morphology was analyzed using a field emission environment scanning electron microscope (SEM, FEI F50). The transmission electron microscopy (TEM) investigations were carried out in a JEOL 2100. Fourier transform infrared (FT-IR) spectra were recorded using a Nicolet 380 FT-IR spectrometer in the wavelength range from 500 to 4000 cm^{-1}. X-ray photoelectron spectroscopy (XPS) tests were carried out in an ESCALAB 250 Xi X-ray photoelectron spectrometer. Elemental analysis was conducted on an Elementar elemental analyzer (EA3000) to determine the element content in Zn-AC and K-AC.

2.3. Electrochemical measurements

The working electrode was prepared by mixing the obtained carbon materials (70 wt%), carbon black (10 wt%), graphite (10 wt%) and polyvinylidene fluoride (PVDF, 10 wt%) in the N-methyl-2-

pyrrolidone (NMP) solvent. The resulting slurry of the above mixture was coated onto a stainless steel grid and vacuum dried at 60 °C for 24 h. The electrochemical experiments were performed using a three-electrode system with the prepared electrode was used as the working electrode, Hg/Hg_2SO_4 and graphite as the reference electrode and counter electrode, respectively, and 1 M H_2SO_4 aqueous solution as the electrolyte. Cyclic voltammetry (CV) and galvanostatic charge–discharge (GCD) were conducted in the potential range from −0.8 to 0.2 V, and electrochemical impedance spectroscopy (EIS) tests were carried out in the frequency range from 10^{-2} Hz to 100 kHz with a CHI 660E electrochemical working station.

3. RESULTS AND DISCUSSION

3.1. Fabrication and characterization of Zn-AC and K-AC

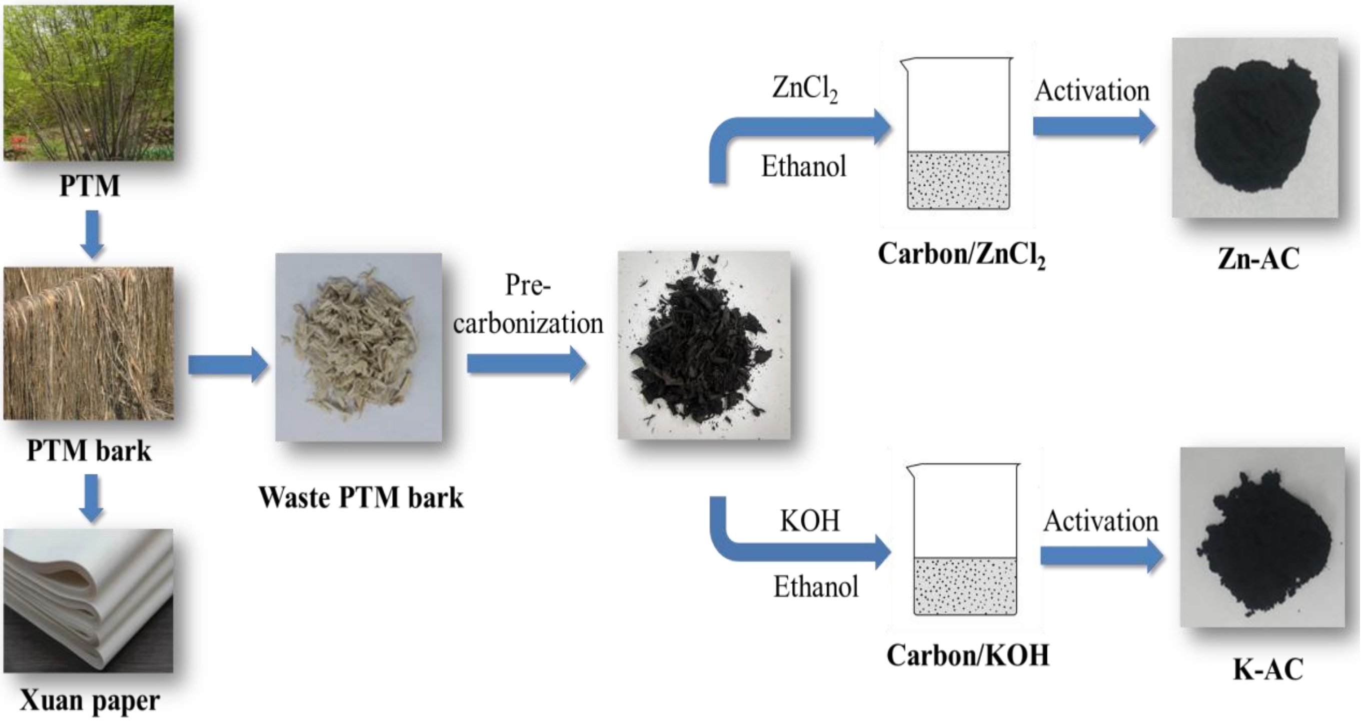

Figure 1. Schematic illustration of the fabrication of Zn-AC and K-AC.

Fig. 1 illustrates the schematic diagram of the fabrication process of Zn-AC and K-AC. First, waste PTM barks are precarbonized at 300 °C, and then the precarbonized barks are mixed with KOH or $ZnCl_2$ in ethanol. Finally, the obtained mixtures are carbonized at 900 °C for 2 h.

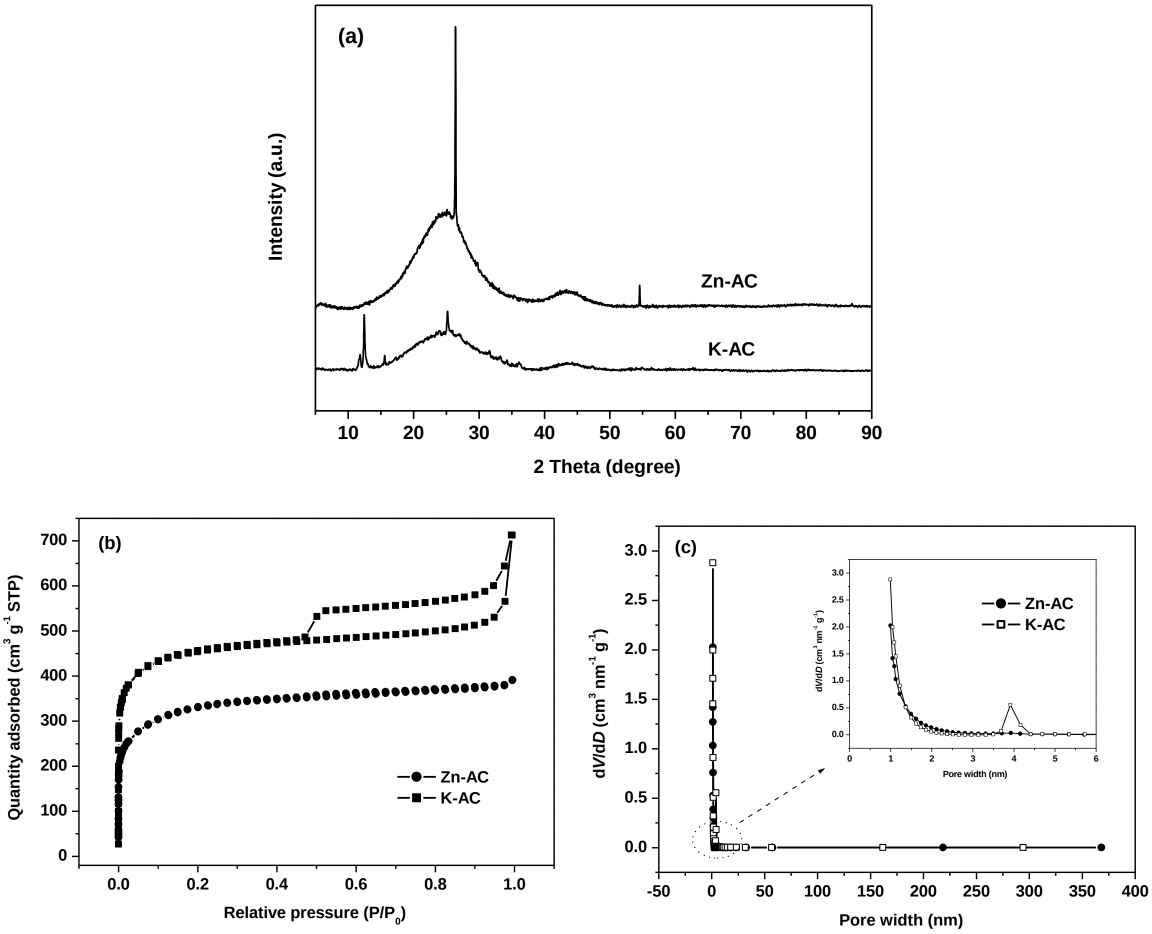

Figure 2. (a) XRD patterns, (b) nitrogen adsorption–desorption isotherms and (c) pore-size distribution curves of Zn-AC and K-AC.

Fig. 2a shows the XRD patterns of Zn-AC and K-AC. Both samples exhibit a broad diffraction peak at approximately 25.1° and a weak diffraction peak at approximately 43.3°, corresponding to the (002) and (100) crystal planes of graphitic domains, respectively [38]. Particularly, for Zn-AC, two more sharp and intense peaks located at approximately $2\theta = 26.5°$ and 54.6° can be assigned to the characteristic (002) and (004) reflection planes of graphite, respectively, which indicate high degree of crystallinity and graphitization in Zn-AC [39]. The XRD result suggests that the crystallographic structure and crystallinity of the waste PTM bark-derived carbon materials are different based on different activation agents.

Fig. 2b presents the nitrogen adsorption-desorption isotherms of Zn-AC and K-AC. According to IUPAC, the N_2 adsorption and desorption isotherms curves of Zn-AC can be classified as type I, in which the adsorption sharply increases at very low relative pressure ($P/P_0 < 0.1$) and then remains at an almost constant value at high relative pressure. No evident hysteresis loop can be observed in the isotherms, indicating the existence of exclusive micropores in Zn-AC. In comparison, K-AC exhibits typical type IV nitrogen adsorption isotherms, with a rapid increase of adsorption, an obvious hysteresis loop and a slight increase tendency appearing at very low relative pressure ($P/P_0 < 0.1$), intermediate relative pressure section (P/P_0 = 0.5−0.9) and high relative pressure region (P/P_0 = 0.95−1.0), respectively, revealing the presence of micropores, mesopores and macropores within K-AC [40,41]. Moreover, the corresponding pore size distributions of Zn-AC and K-AC also demonstrate similar results. As shown in Fig. 2c, the pore size of Zn-AC is distributed in the range from 0.5 to 2.0 nm, which demonstrates the presence of micropores structure in Zn-AC. K-AC possesses a hierarchical porous structure that includes both micropores with diameters between 0.5 and 2.0 nm and small mesopores with a peak centred at 3.9 nm. In addition, the BET surface areas of Zn-AC and K-AC are calculated to be 1210 and 1721 m^2 g^{-1}, respectively, and their total pore volumes are 0.57 and 0.90 cm^3 g^{-1}. This means that the characteristics of the porous structures of the obtained carbon materials are greatly influenced by the activation agents.

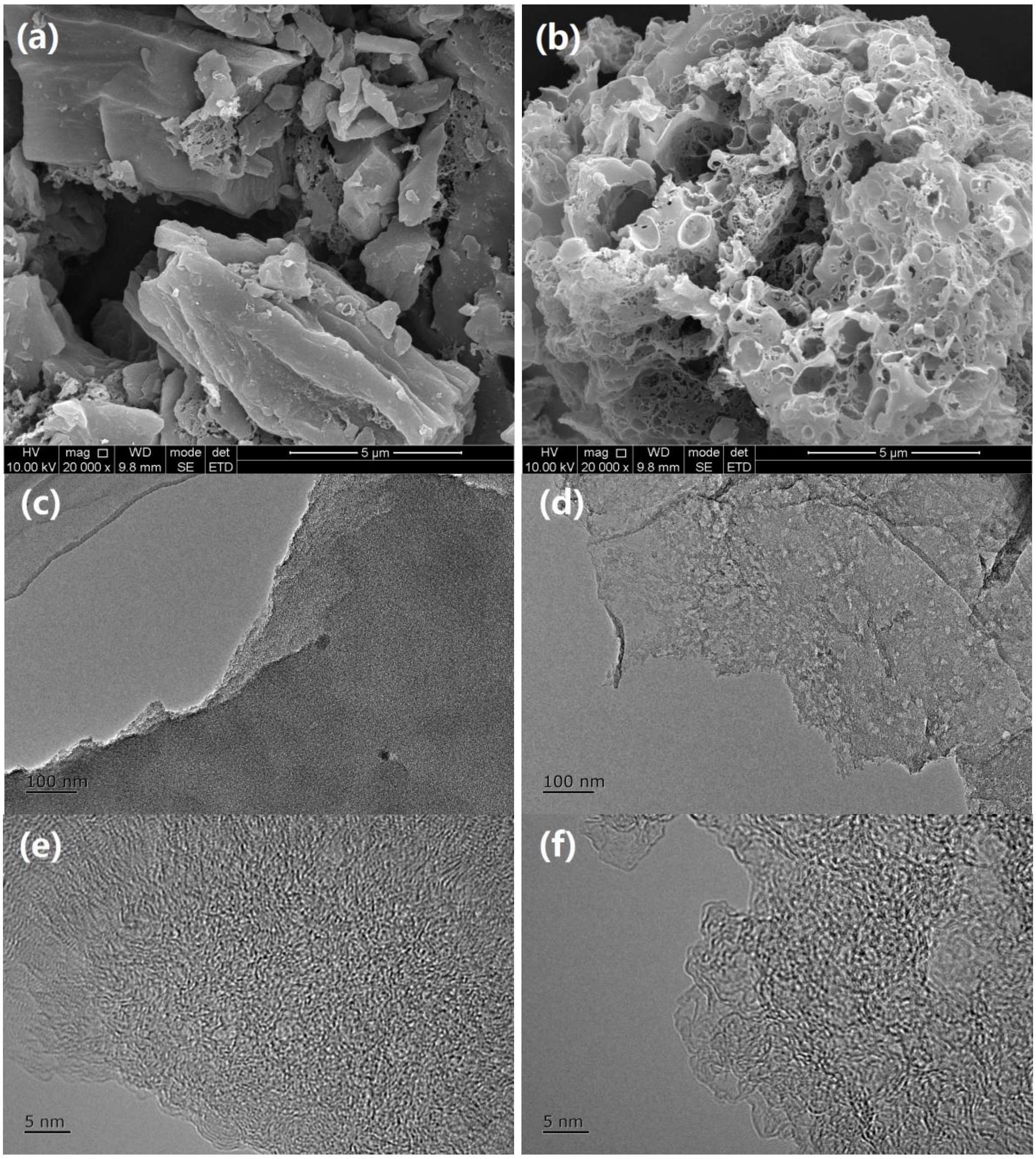

Figure 3. SEM images of (a) Zn-AC and (b) K-AC; TEM images of (c) Zn-AC and (d) K-AC; high-resolution TEM images of (e) Zn-AC and (f) K-AC.

Fig. 3a,b exhibits the SEM images of Zn-AC and K-AC. It can be seen that the morphologies of the samples are completely different. Zn-AC (Fig. 3a) shows the formation of micrometre-sized particles with a rather smooth surface. On the other hand, K-AC (Fig. 3b) exhibits a honeycomb-like structure composed of a unique interconnected macroporous network. The microstructures of Zn-AC and K-AC were examined by TEM. As expected, an apparent nanosized pore structure can be found in Zn-AC (Fig. 3c), and some macro- and mesopores are clearly observed in K-AC (Fig. 3d). In addition, the structural features and the nanometer-sized pores of Zn-AC and K-AC are further confirmed by high-resolution TEM. As shown in Fig. 3e,f, it can be observed that Zn-AC possesses abundant micropores, many distorted graphite-like crystallites and some uniform carbon nanosheets in its microstructure, and K-AC shows a microporous texture and many small mesopores ranging from 2 to 5 nm. The results are in good agreement with XRD and BET analysis data.

Fig. 4a displays the FT-IR spectra of Zn-AC and K-AC. It can be observed that the two samples show similar FT-IR characteristic peaks. The peak located at 3460 cm^{-1} is the typical O–H stretching vibrations of hydroxyl groups or adsorbed water molecules [42]. The weak peak at 2917 cm^{-1} is normally attributed to the stretching vibration of C–H [43].

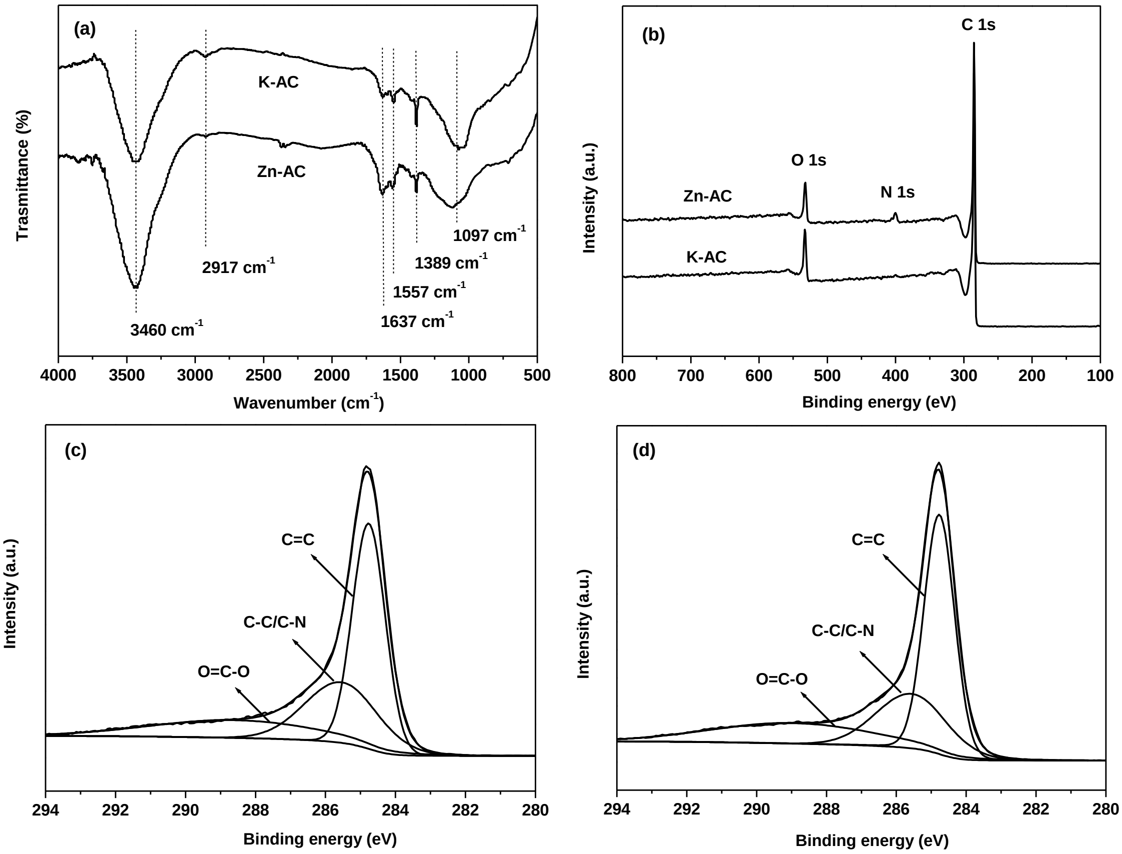

Figure 4. (a) FT-IR spectra and (b) XPS survey spectra of Zn-AC and K-AC; high resolution XPS spectra of C 1s peaks of (c) Zn-AC and (d) K-AC.

The absorption peak at approximately 1389 cm^{-1} can be assigned to the bending vibration of C–H combined with the stretching vibration C–N [44]. Additionally, the absorption peaks at 1637 and

1557 cm^{-1} are assigned to the stretching vibration of C=O/C=C bonds [45,46]. The absorption band occurring at approximately 1097 cm^{-1} can be recognized as the stretching vibration of C–O bonds [47]. The FT-IR results indicate the presence of N and O functional groups in the as-synthesized carbon materials.

XPS was employed to determine the surface elemental compositions of Zn-AC and K-AC, and the analytical results are shown in Fig. 4b-d. From Fig. 4b, it can be seen that Zn-AC displays three peaks with binding energies at 284.8, 400.3 and 531.9 eV, which can be assigned to the C 1s, N 1s and O 1s orbitals, respectively, evidencing the presence of C, N and O elements in Zn-AC. The corresponding atomic percentages of C 1s, N 1s and O 1s calculated according to the XPS analysis are 87.5, 4.5 and 8.0%, respectively. By contrast, for K-AC, the peak belonging to N 1s is very weak and even disappears, indicating a low content of N element in K-AC. The calculated atomic percentage of N 1s is 1.2%, suggesting that KOH activation at high temperature removes a certain amount of nitrogen from carbon materials. The high-resolution C 1s XPS spectra of Zn-AC and K-AC are presented in Fig. 4c and d, respectively. Both samples were deconvoluted into three separate peaks, which correspond to the following functional groups: carbon sp^2 (C=C) at 284.8 eV, carbon sp^3 (C–C) overlapping with sp^2 carbon bound to nitrogen (C–N) at 285.5 eV and carboxylates (O=C–O) at approximately 288.6 eV [41,48]. The XPS data further demonstrate the existence of N and O functional groups on the surface of the obtained carbon skeletons.

Table 1. Elemental analysis results of Zn-AC and K-AC.

Sample	N [wt%]	C [wt%]	H [wt%]
Zn-AC	3.0	70.2	2.8
K-AC	0.3	71.4	2.6

The bulk chemical compositions for Zn-AC and K-AC were further characterized by elemental analysis (EA), and the results are listed in Table 1. It can be observed that Zn-AC shows a relatively high nitrogen content of 3.0 wt%, but K-AC contains only 0.3 wt% nitrogen, which is mainly due to the escape of nitrogen during the KOH activation process at high temperatures. Both EA and XPS analysis results prove that the content of nitrogen in Zn-AC is much higher than that in K-AC. Generally, nitrogen-doping is considered to enhance the electric conductivity, increase the wettability and improve the capacitive performance of carbon materials. Thus, it is expected that Zn-AC will have more excellent electrochemical performance than K-AC.

3.2. Electrochemical properties

The electrochemical properties of Zn-AC and K-AC were first investigated using the CV technique. Fig. 5a and b shows the CV curves of Zn-AC and K-AC at different scan rates ranging from

2 to 100 mV s^{-1}, respectively. It should be noted that both Zn-AC and K-AC exhibit nearly rectangular-shaped CV curves at various scan rates. Even at a high scan rate of 100 mV s^{-1}, the CV curves still retain good rectangular shapes, indicating ideal capacitive behaviors and remarkable rate capability. Moreover, a pair of symmetric redox peaks can be observed in the CV curves of Zn-AC and K-AC at various scan rates, but K-AC exhibits weaker redox peaks than Zn-AC.

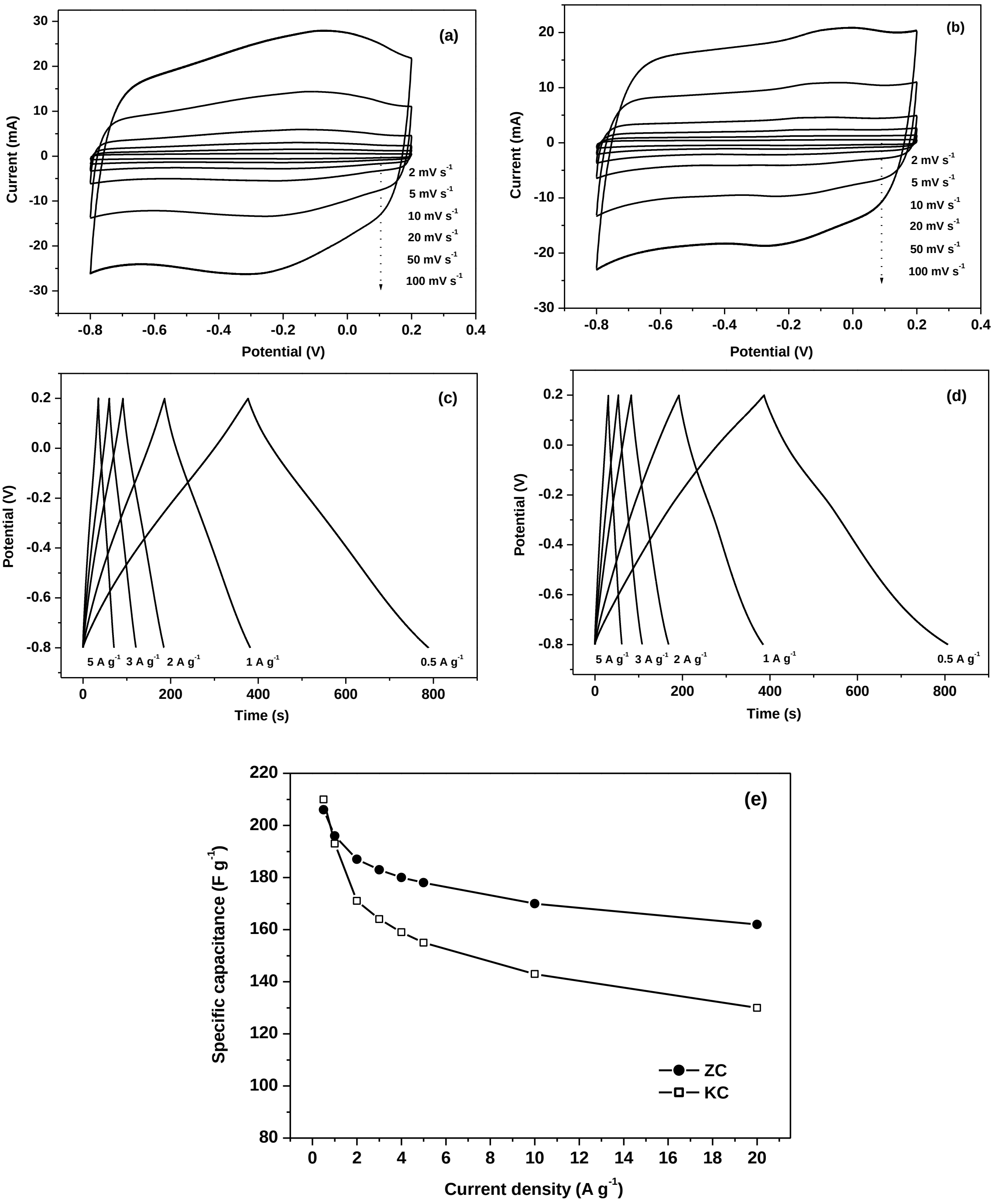

Figure 5. Cyclic voltammograms of (a) Zn-AC and (b) K-AC at different scan rates; galvanostatic charge–discharge curves at various current densities for (c) Zn-AC and (d) K-AC, and (e) the corresponding rate performance comparison of Zn-AC and K-AC.

The behavior indicates that faradic phenomena occur during the electrical double-layer charge-storage mechanism, and the faradic pseudocapacitance is possibly originated from the nitrogen-containing functional groups. Based on the above EA and XPS analysis results, the content of nitrogen in Zn-AC is higher than that in K-AC. Thus, the additional nitrogen functional groups would provide more pseudocapacitive contribution for Zn-AC. The calculated specific capacitances of Zn-AC and K-AC from the CV curves are 197 F g^{-1} and 185 F g^{-1}, respectively, at a scan rate of 2 mV s^{-1}. Moreover, the specific capacitance values decrease with the increase in scan rate. However, even when the scan rate increases to 100 mV s^{-1}, Zn-AC still gives a high specific capacitance of 160 F g^{-1}, indicating that the good rate capability is due to fast electrolyte ions diffusion kinetics. In contrast, the specific capacitance of K-AC is less than 130 F g^{-1} at 100 mV s^{-1}.

The supercapacitive behavior of Zn-AC and K-AC was further measured by galvanostatic charge–discharge (GCD) measurements, and the GCD curves at different current densities are shown in Fig. 5c and d. Consistent with the results from CV studies, the GCD curves of Zn-AC (Fig. 5c) and K-AC (Fig. 5d) show an approximately symmetric triangular shape and a slight curvature characteristic, implying a pseudocapacitive behavior along with the double-layer contribution. Moreover, for Zn-AC, no obvious IR drop can be observed at various current densities, indicating low polarization resistance and superior capacitive behavior. However, K-AC exhibits a small initial potential drop at a low current density of 0.5 A g^{-1}, and the initial potential drop increases gradually as the current density increases, suggesting limited kinetics for the charge-storage processes.

Fig. 5e gives the galvanostatic specific capacitance values of Zn-AC and K-AC calculated from the GCD curves at various current densities. Notably, Zn-AC and K-AC yield similar values of the specific capacitance at low current densities in the range of 0.5 to 1 A g^{-1}. With the current density increasing, the specific capacitance values of Zn-AC gradually decrease but always higher than those of K-AC at the same current density. Zn-AC still maintains a high specific capacitance of 162 F g^{-1} at a high current density of 20.0 A g^{-1} with a capacitance retention of 79% relative to 206 F g^{-1} at 0.5 A g^{-1}. By contrast, K-AC preserves only 62% of its specific capacitance (from 210 to 130 F g^{-1}) as the current density increases from 0.5 to 20 A g^{-1}.

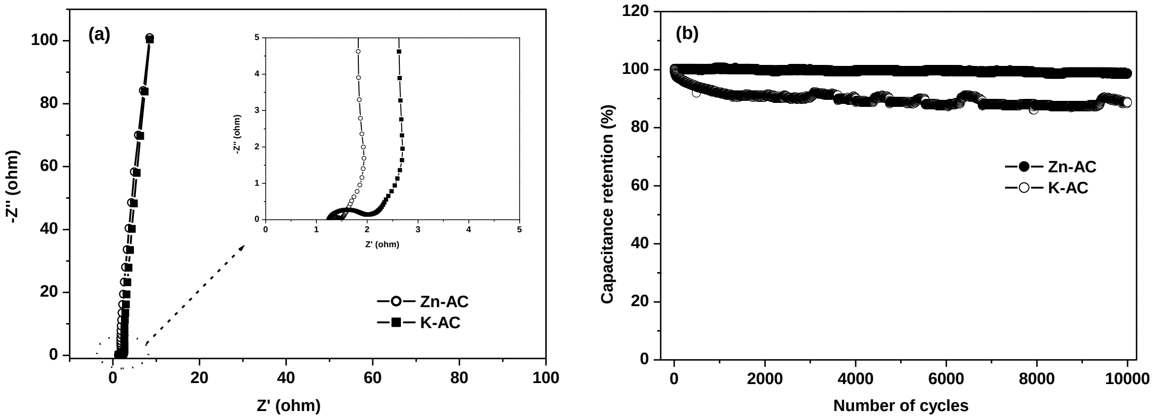

Figure 6. (a) EIS spectra and (b) cycling performance comparison of Zn-AC and K-AC.

The results are in good agreement with the results from CV studies, and both indicate that Zn-AC possesses a better rate capability than K-AC. The excellent rate performance for Zn-AC is mainly attributed to the relatively high content of nitrogen-containing functional groups, which can enhance the electric conductivity and improve the surface wettability and allow the electrolyte ions to easily diffuse into and out of the inner pores of carbon materials.

Fig. 6a shows the EIS spectra of Zn-AC and K-AC. At very high frequencies, the intercepts at the real axis Z' are nearly the same value for the two samples, implying Zn-AC and K-AC exhibit almost the same combination resistance of the intrinsic resistance of the active material, the ionic resistance of the electrolyte and the contact resistance at the interface between the active material and the current collector. At high frequencies, the semicircle is typically associated with the interface charge transfer processes of the electrode. The diameter of the semicircle can be recognized as the charge-transfer resistance (Rct) at the interface of the electrode and the electrolyte [49]. Apparently, Zn-AC exhibits smaller diameter than K-AC, suggesting a lower R_{ct}.

Table 2. Comparison of biomass-derived carbon materials as electrodes for supercapacitor application.

Precursor	Activation agent	Electrolyte	Capacitance retention	Ref.
Jujun grass	KOH	6 M KOH	88% after 2000 cycles	34
Platanus seed fibers	KOH	6 M KOH	97% after 10,000 cycles	35
Soybean root	KOH	6 M KOH	98% after 10,000 cycles	50
Flour food	KOH	6 M KOH	95% after 3,000 cycles	51
Corncob	KOH	6 M KOH	97% after 5,000 cycles	52
Banana fibers	KOH	1 M Na_2SO_4	70% after 5,000 cycles	53
Banana fibers	$ZnCl_2$	1 M Na_2SO_4	88% after 5,000 cycles	53
Silk	$ZnCl_2$	1 M $LiPF_6$	91% after 10,000 cycles	33
Coffee beans	$ZnCl_2$	1 M H_2SO_4	95% after 5,000 cycles	54
Coconut shell	$ZnCl_2$	6 M KOH	99.5% after 5000 cycles	55
Sunflower marrow	$ZnCl_2$	0.5 M Na_2SO_4	97% after 5,000 cycles	56
PTM bark	KOH	1 M H_2SO_4	89% after 10,000 cycles	This work
PTM bark	$ZnCl_2$	1 M H_2SO_4	99% after 10,000 cycles	This work

The cycling performance of Zn-AC and K-AC was investigated by galvanostatic charge–discharge cycles up to 10,000 cycles at a current density of 3 A g^{-1}, and the variation of the capacitance retention ratio of both samples as a function of the cycle number is shown in Fig. 6b. For K-AC, a fractional decrease in the specific capacitance can be found during the initial 1000 cycles. Thereafter, the specific capacitance decreases slightly. After 10,000 cycles, the specific capacitance remains approximately 89% of the initial value. In contrast, the specific capacitance of Zn-AC remains at an almost constant value during the cycles. Even after 10,000 cycles, it still retains a capacitance retention ratio of approximately 99%. The results demonstrate that Zn-AC possesses more excellent cycling stability than K-AC. The superior cycle performance of Zn-AC is mainly attributed to the stable self-doped nitrogen functionalities, which significantly enhance the structural stability of Zn-AC during the long-term electrochemical cycling process. Table 2 summarizes the cycling performance of biomass-derived carbon electrodes for supercapacitor application. Notably, Zn-AC shows a more excellent cycling stability than the most reported biomass-derived carbon materials. The comparison further confirms that such waste PTM bark-derived carbon material, obtained by the $ZnCl_2$ activated method, is a promising electrode material for high-performance supercapacitors.

4. CONCLUSION

In this paper, we proposed a new biomass source of waste PTM bark for preparing nitrogen self-doped carbon materials. The obtained KOH activated carbon (K-AC) possessed a hierarchical porous structure with a high specific surface area of 1721 m^2 g^{-1} and small amount of nitrogen (0.3 wt%). Compared with K-AC, $ZnCl_2$-activated carbon (Zn-AC) showed a micropore structure with a narrow pore size distribution (0.5–2.0 nm) and a higher nitrogen content of 3.0 wt%, indicating that the characteristics of porous structures and the content of nitrogen in the carbon materials were greatly influenced by the activation agents. The electrochemical measurement results demonstrated that the as-prepared Zn-AC possessed a high specific capacitance of 206 F g^{-1} at 0.5 A g^{-1}, good rate performance and excellent cycle stability with capacitance retention of 99% over 10,000 cycles. In contrast, K-AC retained only approximately 89% of the initial capacitance value after 10,000 cycles. The superior cycle performance of Zn-AC was mainly attributed to the stable self-doped nitrogen functionalities, which significantly enhanced the structural stability of Zn-AC during the long-term electrochemical cycling process. Thus, the waste PTM bark-derived nitrogen self-doped carbon material is a promising electrode material for highly stable supercapacitors, and $ZnCl_2$ is an efficient activation agent for the preparation of nitrogen self-doped porous carbon materials.

ACKNOWLEDGEMENTS
The authors would like to thank the National Natural Science Foundations of China (Grant No. 21706048, U1632151), China Postdoctoral Science Foundation (2016M590565), the Fundamental Research Fund for the Central Universities (JZ2016HGTA0683), and the grants from Startup Foundation of Hefei University of Technology (JZ2015HGBZ0530, XC2016JZBZ06).

References

1. P. Simon and Y. Gogotsi, *Nat. Mater.*, 7 (2008) 845.
2. Y. G. Wang, Y. F. Song and Y. Y. Xia, *Chem. Soc. Rev.*, 45 (2016) 5925.
3. L. L. Zhang and X. S. Zhao, *Chem. Soc. Rev.*, 38 (2009) 2520.
4. D. Puthusseri, V. Aravindan, S. Madhavi and S. Ogale, *Energy Environ. Sci.*, 7 (2014) 728.
5. R. J. Mo, Y. Zhao, M. Wu, H. M. Xiao, S. Kuga, Y. Huang, J. P. Li and S. Y. Fu, *RSC Adv.*, 6 (2016) 59333.
6. H. M. Ji, T. Wang, Y. Liu, C. L. Lu, G. Yang, W. P. Ding and W. H. Hou, *Chem. Commun.*, 52 (2016) 12725.
7. Y. Y. Li, Z. S. Li and P. K. Shen, *Adv. Mater.*, 25 (2013) 2474.

8. M. Inagaki, H. Konno and O. Tanaike, *J. Power Sources*, 195 (2010) 7880.
9. X. J. Wei, Y. B. Li and S. Y. Gao, *J. Mater. Chem. A*, 5 (2017) 181.
10. X. H. Wang, Y. H. Li, F. L. Lou, M. E. M. Buan, E. Sheridan and D. Chen, *RSC Adv.*, 7 (2017) 23859.
11. C. Shi, L. T. Hu, K. Guo, H. Q. Li and T. Y. Zhai, *Adv. Sustainable Syst.*, 1 (2017) 1600011.
12. Y. L. Huang, H. H. Cheng, D. Shu, J. Zhong, X. N. Song, Z. P. Guo, A. M. Gao, J. N. Hao, C. He and F. Y. Yi, *Chem. Eng. J.*, 320 (2017) 634.
13. X. L. Li, Y. J. Zhao, Y. Bai, X. Y. Zhao, R. H. Wang, Y. C. Huang, Q. H. Liang and Z. H. Huang, *Electrochim. Acta*, 230 (2017) 445.
14. J. Wang, L. F. Shen, B. Ding, P. Nie, H. F. Deng, H. Dou and X. G. Zhang, *RSC Adv.*, 4 (2014) 7538.
15. R. R. Rajagopal, L.S. Aravind, R. Rajarao, B. R. Bhat and V. Sahajwalla, *Electrochim. Acta*, 211 (2016) 488.
16. L. F. Chen, Y. Lu, L. Yu and X. W. (David) Lou, *Energy Environ. Sci.*, 10 (2017) 1777.
17. K. Xiao, L. X. Ding, G. X. Liu, H. B. Chen, S. Q. Wang and H. H. Wang, *Adv. Mater.*, 28 (2016) 5997.
18. L. Z. Sheng, L. L. Jiang, T. Wei, Z. Liu and Z. J. Fan, *Adv. Energy Mater.*, (2017) 1700668.
19. Y. J. Cai, Y. Luo, Y. Xiao, X. Zhao, Y. R. Liang, H. Hu, H.W. Dong, L. Y. Sun, Y. L. Liu and M. T. Zheng, *ACS Appl. Mater. Interfaces*, 8 (2016) 33060.
20. J. Yan, Q. Wang, T. Wei and Z. J. Fan, *Adv. Energy Mater.*, 4 (2014) 157.
21. J. P. Paraknowitsch and A. Thomas, *Energy Environ. Sci.*, 6 (2013) 2839.
22. L. F. Chen, X. D. Zhang, H. W. Liang, M. G. Kong, Q. F. Guan, P. Chen, Z. Y. Wu and S. H. Yu, *ACS Nano*, 6 (2012) 7092.
23. J. T. Hu, J. Yang, Y. D. Duan, C. K. Liu, H. T. Tang, L. P. Lin, Y. Lin, H. B. Chen and F. Pan, *Chem. Commun.*, 53 (2017) 857.
24. F. Y. Hu, J. Y. Wang, S. Hu, L. F. Li, G. Wang, J. S. Qiu and X. G. Jian, *Nanoscale*, 8 (2016) 16323.
25. G. Qu, S. F. Jia, H. Wang, F. Cao, L. Li, C. Qing, D. M. Sun, B. X. Wang, Y. W. Tang and J. B. Wang, *ACS Appl. Mater. Interfaces*, 8 (2016) 20822.
26. L. N. Han, X. Wei, Q. C. Zhu, S. M. Xu, K. X. Wang and J. S. Chen, *J. Mater. Chem. A*, 4 (2016) 16698.
27. Z. Ling, Z. Y. Wang, M. D. Zhang, C. Yu, G. Wang, Y. F. Dong, S. H. Liu, Y. W. Wang and J. S. Qiu, *Adv. Funct. Mater.*, 26 (2016) 111.
28. Y. F. Zhao, W. Ran, J. He, Y. F. Song, C. M. Zhang, D. B. Xiong, F. M. Gao, J. S. Wu and Y. Y. Xia, *ACS Appl. Mater. Interfaces*, 7 (2015) 1132.
29. E. C. Hao, W. Liu, S. Liu, Y. Zhang, H. L. Wang, S. G. Chen, F. L. Cheng, S. P. Zhao and H. Z. Yang, *J. Mater. Chem. A*, 5 (2017) 2204.
30. A. Sanchez-Sanchez, M. T. Izquierdo, S. Mathieu, J. González-Álvarez, A. Celzard and V. Fierro, *Green Chem.*, 19 (2017) 2653.
31. Z. J. Sun, S. J. Wang, L. L. Yan, M. Xiao, D. M. Han and Y. Z. Meng, *J. Power Sources*, 324 (2016) 547.
32. H. J. Liu, X. M. Wang, W. J. Cui, Y. Q. Dou, D. Y. Zhao and Y. Y. Xia, *J. Mater. Chem.*, 20 (2010) 4223.
33. J. H. Hou, C. B. Cao, F. Idrees and X. L. Ma, *ACS Nano*, 9 (2015) 2556.
34. Y. C. Liu, B. B. Huang, X. X. Lin and Z. L. Xie, *J. Mater. Chem. A*, 5 (2017) 13009.
35. H. Tan, X. N. Wang, D.D. Jia, P. Hao, Y. H. Sang and H. Liu, *J. Mater. Chem. A*, 5 (2017) 2580.
36. Y. Yang, J. H. Zha, L. Liu and N. Y. Yuan, Int. J. Electrochem. Sci., 12 (2017) 7326.
37. N. S. M. Nor, M. Deraman, M. Suleman, M. R. M. Jasni, J. G. Manjunatha, M. A. R. Othman, S. A. Shamsudin, Int. J. Electrochem. Sci., 12 (2017) 2520.
38. Z. J. Zhang, Q. Wang, Y. Q. Zhu and X. Y. Chen, *Carbon*, 100 (2016) 564.

39. H. Z. Zhang, W. D. Qiu, Y. F. Zhang, Y. Han, M. H. Yu, Z. F. Wang, X. H. Lu and Y. X. Tong, *J. Mater. Chem. A*, 4 (2016) 18639.
40. M. Kruk and M. Jaroniec, *Chem. Mater.*, 13 (2001) 3169.
41. P. Hao, Z. H. Zhao, Y. H. Leng, J. Tian, Y. H. Sang, R. I. Boughton, C. P. Wong, H. Liu and B. Yang, *Nano Energy*, 15 (2015) 9.
42. M. Karnan, K. Subramani, N. Sudhan, N. Ilayaraja and M. Sathish, *ACS Appl. Mater. Interfaces*, 8 (2016) 35191.
43. M. K. Song, Y. G. Zhang and E. J. Cairns, *Nano Lett.*, 13 (2013) 5891.
44. H. Denga, G. Li, H. Yang, J. Tang and J. Tang, *Chem. Eng. J.*, 163 (2010) 373.
45. Z. Li, K. K. Guo and X. L. Chen, *RSC Adv.*, 7 (2017) 30521.
46. Z. Lei, J. Zhang and X. S. Zhao, *J. Mater. Chem.*, 22 (2012) 153.
47. R. R. Liu, H. M. Zhang, S. W. Liu, X. Zhang, T. X. Wu, X. Ge, Y. P. Zang, H. J. Zhao and G. Z. Wang, *Phys. Chem. Chem. Phys.*, 18 (2016) 4095.
48. Z. J. Sun, M. Xiao, S. J. Wang, D. M. Han S. Q. Song, G. H. Chen and Y. Z. Meng, *J. Power Sources*, 285 (2015) 478.
49. Z. J. Sun, H. Y. Chen, D. Shu, C. He, S. Q. Tang and J. Zhang, *J. Power Sources*, 203 (2012) 233.
50. N. N. Guo, M. Li, Y. Wang, X. K. Sun, F. Wang and R. Yang, *ACS Appl. Mater. Interfaces*, 8 (2016) 33626
51. C. Z. Zhan, X. L. Yu, Q. H. Liang, W. Liu, Y. B. Wang, R. T. Lv, Z. H. Huang and F. Y. Kang, RSC Adv., 6 (2016) 89391.
52. L. L. Wang, Y. T. Li, K. L. Yang, W. Q. Lu, J. G. Yu, J. Gao, G. Liao,Y. N. Qu, X. F. Wang, X. F. Li and Z. Yin, *Int. J. Electrochem. Sci.*, 12 (2017) 5604.
53. V. Subramanian, C. Luo, A. Stephan, K. Nahm, S. Thomas and B. Q. Wei, J. Phys. Chem. C, 111 (2007) 7527.
54. T. E. Rufford, D. Hulicova-Jurcakova, Z. H. Zhu and G. Q. Lu, Electrochem. Commun., 10 (2008) 1594.
55. L. Sun, C. Tian, M. Li, X. Meng, L. Wang, R. Wang, J. Yin and H. Fu, J. Mater. Chem. A, 1 (2013) 6462.
56. K. J. Sun, Q. Yang, Y. P. Zheng, G. H. Zhao, Y. R. Zhu, X. P. Zheng and G. F. Ma, *Int. J. Electrochem. Sci.*, 12 (2017) 2606.